THERMAL AND DENSITY STRUCTURE OF POLAR PLUMES

I. *Analysis of EUV Observations with a Multilayer Cassegrain Telescope*

A. B. C. WALKER, JR., C. E. DEFOREST
Departments of Physics and of Applied Physics and Center for Space Science and Astrophysics, Stanford University, Stanford, CA 94305, U.S.A.

RICHARD B. HOOVER
Space Science Laboratory, NASA Marshall Space Flight Center, AL 35812, U.S.A.

and

TROY W. BARBEE, JR.
Lawrence Livermore National Laboratory, Livermore, CA 94550, U.S.A.

(Received 29 December, 1992; in revised form 14 April, 1993)

Abstract. Normal incidence multilayer coated EUV/XUV optical systems provide a powerful technique for the study of the structure of the solar corona. Such systems permit the imaging of the full solar disk and corona with high angular resolution in narrow wavelength bands that are dominated by a single line or a line multiplet excited over a well defined range of temperatures. We have photometrically analysed, and derived temperature and density information from, images of polar plumes obtained with a multilayer Cassegrain telescope operating in the wavelength interval $\lambda = 171$ to 175 Å, which is dominated by Fe IX and Fe X emission. This observation was obtained in October 1987, and is the first high resolution observation of an astronomical object obtained with normal incidence multilayer optics techniques. We find that photometric data taken from this observation, applied to a simple, semi-empirical model of supersonic solar wind flow, are consistent with the idea that polar plumes are a source of the solar wind. However, we are not able to uniquely trace high speed streams to polar plumes. The temperatures that we observed are typically ~1 500 000 K for both the plumes and the interplume regions, with the plume temperatures slightly higher than those of the surrounding atmosphere. Typical electron densities of the plume and interplume regions, respectively, are 5×10^9 cm^{-3} and 1×10^8 cm^{-3} at the limb of the Sun.

1. Introduction

Polar plumes are believed to be a major source of the solar wind, and may provide the mechanism responsible for the high speed solar wind streams associated with coronal holes. Withbroe (1986) has reviewed models of polar plumes and pointed out the importance of high-resolution (~1 arc sec) observations of polar plumes to an understanding of the physics of coronal holes. Previous observations of polar plumes on Skylab in the soft X-ray and EUV have been limited to resolutions of several arc sec, and a distance of 0.4 solar radii or less above the limb. Our 1987 observations recorded measurable plume EUV emissions out to 0.5 solar radii above the limb with a resolution of approximately 1 arc sec.

We have reported previously on our observations of the structure of the corona on October 23, 1987 (Walker *et al.*, 1988a). Figure 1 is the first high resolution image of the corona obtained using the technique of multilayer coated normal incidence

Solar Physics **148:** 239–252, 1993.

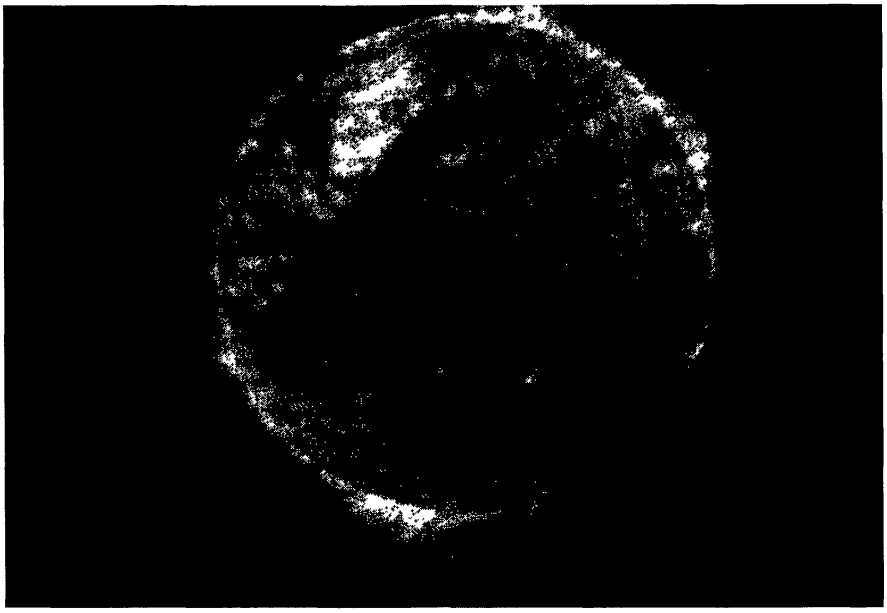

Fig. 1. The solar corona photographed in the emission of the resonance lines of Fe XI and Fe X at ~171–175 Å, on 23 October, 1987 at 18:09 UT. The length of the exposure was 200 s. Coronal plumes are clearly seen at the north (*top*) and south (*bottom*) polar coronal holes. The plumes at the north pole were vignetted by the ultraviolet filter holder.

optics. Walker *et al.* (1988a, b) and Lindblom *et al.* (1988) have described in some detail the instrumentation used, including the techniques used to prepare the optical surfaces, and to fabricate and test the multilayer coatings. The scientific principles and the technology associated with multilayer coatings have been described by Barbee (1985, 1989), and the application of multilayer optics to astronomical observations has been addressed by Walker *et al.* (1990) and Walker, Hoover, and Barbee (1992a). The XUV-100 photographic films used to record the observations are described by Hoover *et al.* (1988).

The bandpass of the telescope which obtained the image of Figure 1 is shown in Figure 2(a), superimposed on the solar spectrum; and the thermal response of the telescope to the coronal plasma, as calculated by DeForest *et al.* (1991) is shown in Figure 2(b). Analysis of previous observations of polar plumes by Skylab (Bohlin, Sheeley, and Tousey, 1978; Ahmad and Withbroe, 1978) have indicated that the temperature of these structures is ~1 000 000 to 1 200 000 K, suggesting that the Fe IX/Fe X observations should be well suited to the study of plumes. The resolution of the original image used for Figure 1, ~1.1 arc sec (Walker *et al.*, 1988a) is considerably finer than that of the Skylab observations (~3–5 arc sec). Furthermore, the multilayer telescope had extremely low scatter, and the high contrast, high resolution images produced permit the plumes and interplume regions to be well differentiated. Figure 3 is an enlarged view of the region near the south pole, from Figure 1; several plumes and inter-plume regions are clearly visible.

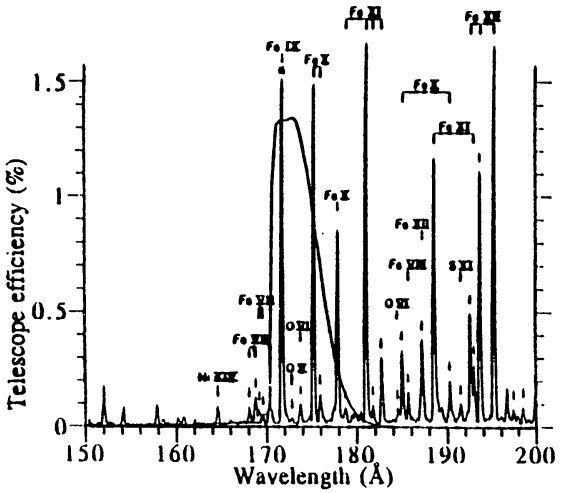

Fig. 2a. Spectral response of the multilayer Cassegrain telescope superimposed on the solar spectrum (as measured by Malinovsky and Hénoux, 1973).

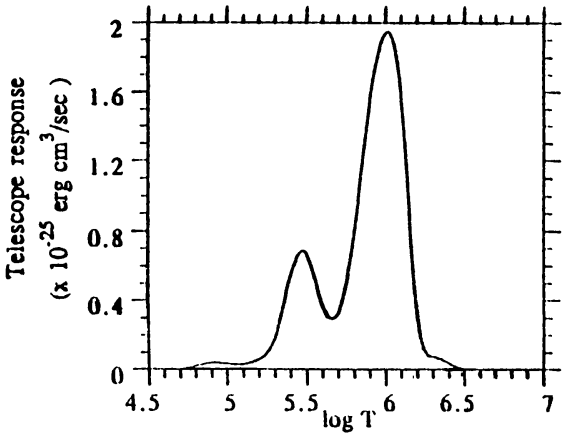

Fig. 2b. Response of the Cassegrain multilayer telescope to an isothermal plasma of unit emission measure.

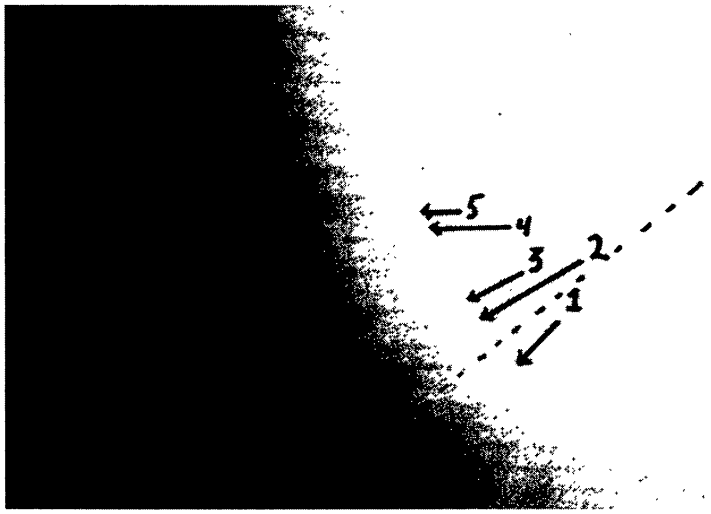

Fig. 3. Detail from Figure 1, near the solar south pole. Several plumes and interplume regions are labelled.

We note that a possible ambiguity in the interpretation of the observations of Figure 1 arises because the telescope band pass includes, in addition to the dominant Fe IX and Fe X lines at 171.075 and 174.534 Å, respectively, weaker lines of O V (172.174) and O VI (172.936 and 173.081 Å) (Doschek and Cowen, 1984). The peak response of the telescope to these lines, which occurs for plasmas at $\sim 3 \times 10^5$ K, is less than 35% of the peak response to the cluster of Fe lines, which is at 1 100 000 K (DeForest *et al.*, 1990). However, for the full solar disk, the contribution to the flux by the oxygen lines in this bandpass is less than 4%

(Malinovsky and Héroux, 1973). Nevertheless, their contribution could dominate the images of structures with large emission measure below 500 000 K. We believe that our analysis of the height variation of plume EUV emission eliminates this possibility, by constraining the temperature of the plumes.

We derive temperature primarily from our analysis of the scale height of the emission observed, however, limits can be placed on the plume temperature, by a second image, taken simultaneously by a telescope operating at the He II Lyman β line at 256 Å. This bandpass also includes strong lines of Fe XIV, as well as several weaker lines. Figure 4(a) is an image obtained with the Herschelian multilayer telescope with bandpass centered at 256 Å, and Figure 4(b) is the temperature response of this telescope. The telescope has a strong response for material at 80 000 and 2 500 000 K, and a relatively weak response for material at 1 000 000 K (DeForest *et al.*, 1990). As expected, the plumes are not visible in Figure 4(a).

2. Calibration and Data Reduction

To perform quantitative analysis on the flight images, the original flight negatives were digitized using the Eikonix microdensitometer at the National Center for Atmospheric Research in Boulder, Colorado. Because of the granular nature of film, a tradeoff exists between high spatial resolution and high signal-to-noise ratio in photometric values. The images were digitized at a resolution of 11.8 microns, corresponding to 1.2 arc sec, at a depth of 8 bits. At this resolution, film grain is clearly visible. The digitized value of each pixel from the Eikonix is directly proportional to the transmission ratio of the film, yielding an image dynamic range of ~24 dB.

Photometric calibration of the film was performed at the National Institute of Standards and Technology (NIST) SURF-II synchrotron, and at Los Alamos National Laboratory, and has been described by Hoover *et al.* (1990a, 1992). The exposed spots obtained through the calibration process were digitized at NCAR, along with the flight film. A H&D curve was iteratively fit to the digitized images, using the thick emulsion model of Henke *et al.* (1984) and the exposure data taken during the film calibration. There are three free parameters in this model: $D_{\min}$, the film fog level; I_{toe}, the lowest resolvable intensity; and γ, the film's contrast factor. The model H&D curve is

$$D = D_{\min} + \gamma \log\left(1 + \frac{I}{I_{\text{toe}}}\right) . \tag{1}$$

Henke *et al.* derive these parameters in terms of a microscopic model of the film emulsion. Rather than explicitly modelling the microscopic film behavior for each of our film types, we empirically fit these macroscopic film parameters to the measured film response data.

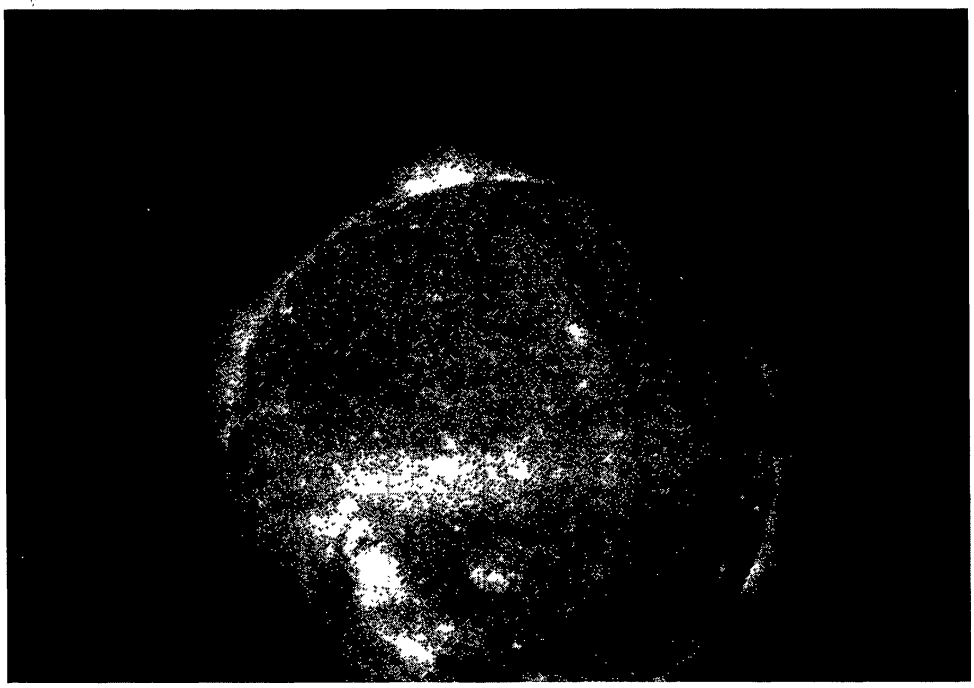

Fig. 4a. The Sun in the wavelength interval ~245 Å < λ < 265 Å on 23 October, 1987 at 18:09 UT. The chromospheric network is seen in He II, while active regions are dominated by emissions from Fe XIV.

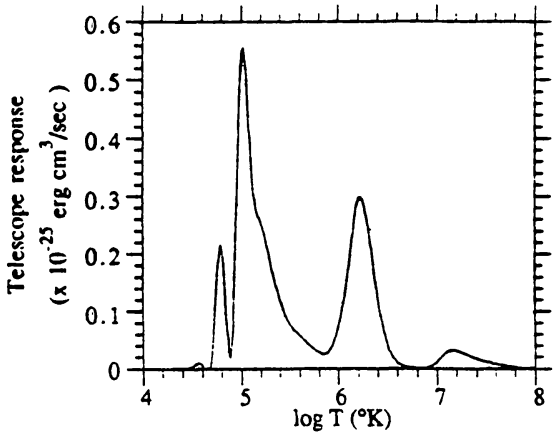

Fig. 4b. The thermal response of the 256 Å Herschellian Telescope.

The efficiency of the telescope was measured using the SURF-II synchrotron, and beamline IV at the Stanford Synchrotron Radiation Laboratory (SSRL). Hoover *et al.* (1990b) have described the procedures used and the results obtained. We calculated the temperature response kernel of the telescope, using the solar emission data calculated by Mewe, Gronenschild, and van den Oord (1985) and Landini and Fossi (1990).

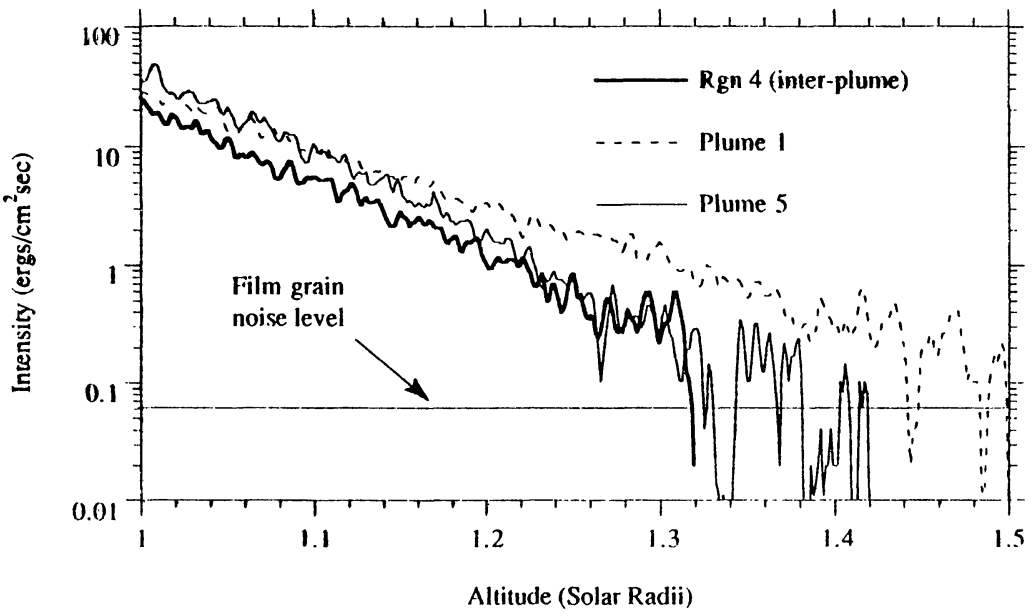

Fig. 5. Measured EUV intensities at the film plane, as a function of height above the center of the Sun, for three of the regions in Figure 3. Note that the traces are nearly straight on this semi-log graph, indicating that the plumes are nearly isothermal; in a uniform gravitational field, the density (and emission) from an isothermal, static plume would fall exponentially with height.

Radial exposure profiles were extracted from the digitized image shown in Figure 3, using the image calibration curve described above. For each plume, the photon flux on the film was calculated along a line from the intersection of the plume profile with the limb of the Sun, to the end of the visible plume. Position was parametrized by height above the limb of the Sun. Because of the level of film grain present, each datapoint in the radial flux curve was averaged over a five pixel long line perpendicular to the direction of the plume. Figure 5 shows several of the flux curves generated in this manner. To extract plasma diagnostic information from these curves, the semi-empirical plume model described below was fit to each plume.

3. Plume Models

We modelled the observed polar plumes as radial (i.e., truncated conical), circular cross-section, columns of plasma embedded in a coronal hole, the interplume region (Figure 6). Aside from the difference between the interplume atmosphere and the plume itself, we assumed that all variables depend only on radius from the center of the Sun. We anticipate that the interplume material is at lower temperature and density compared to the plume material.

To model the solar wind, Parker (1956, 1963) introduced a simple steady-state, single-fluid dynamic model of radial coronal behavior, in which there are three independent variables: temperature, particle density, and radial velocity. We

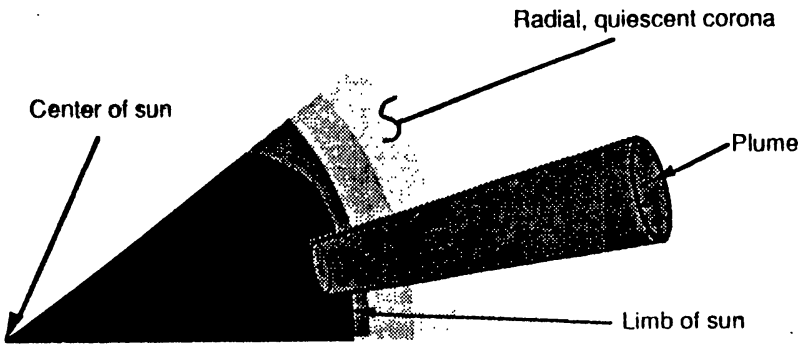

Fig. 6. Simple polar plume geometry. The plume is modelled as a truncated cone (whose density and temperature vary only with radius), embedded in a spherically-symmetric, optically thin interplume coronal atmosphere.

applied this simple model to our plume observations. Assuming the plume is in steady state, we consider three equations:

– conservation of mass as the gas expands,

$$\frac{\partial}{\partial r}(n_p r^2 v) = -\frac{\partial}{\partial t}(n_p r^2) = 0\,, \tag{2}$$

– conservation of momentum,

$$v\frac{\partial v}{\partial r} + \frac{1}{n_p \mu_{\rm eff}}\frac{\partial P}{\partial r} + \frac{G m_\odot}{r^2} = -\frac{\partial v}{\partial t} = 0\,, \tag{3}$$

and the ideal gas law,

$$P = k_B t n_p\,, \tag{4}$$

where n_p is the total particle density ($\approx 2n_e$), $\mu_{\rm eff}$ is the average particle mass ($\approx \mu_H/2$), r is radius from the center of the Sun, v is radial velocity, P is the pressure of the plasma considered as an ideal gas, G is the universal gravitational constant, and k_B is Boltzmann's constant.

The energy balance of the plume must be described, to complete the set of equations. Rather than directly modelling heat input by the coronal heating mechanism, and energy loss by conduction and radiation, we follow Parker and assume a polytrope equation of state for the corona,

$$T = T_0\left(\frac{\rho}{\rho_0}\right)^{\alpha-1} \quad \text{or} \quad P = P_0\left(\frac{\rho}{\rho_0}\right)^{\alpha}\,, \tag{5}$$

where T_0 and ρ_0 are initial conditions to the equations, and α describes the balance between heating, radiation, and conductive energy loss that occurs in the corona. Setting $\alpha = 1$ is equivalent to letting the corona be isothermal, while setting

$\alpha = \frac{5}{3}$ treats the plume as an ideal gas that is expanding adiabatically. Using (5) to eliminate P from (2)–(4), we obtain three differential equations in three unknowns, allowing a three-parameter set of solutions for any given value of α.

Assuming that the coronal plasma is optically thin at the wavelength of observation, and that the observed radiation is collisional line radiation, we can calculate how a given X-ray telescope would respond to a particular modelled volume of plasma, according to the equation (DeForest *et al.*, 1990)

$$\Phi(x, y) = \frac{\pi}{4f^2}\mathbf{V}(x, y)\int \mathrm{d}s\, n_e^2(s, x, y)K_{\mathrm{tel}}(T_e(s, x, y))\,, \tag{6}$$

where Φ is the X-ray flux at the film plane of the telescope; f is the f-ratio of the telescope; x and y index the location on the film plane; $\mathbf{V}$ is the vignetting function, which is negligible for this image; s is a parameter along the line of sight; n_e and T_e are the electron density and temperature of the plasma; and K_{tel} is the temperature response kernel of the telescope, a measure of how strongly the solar plasma emits in the telescope's wavelength passband. Because of the spherical symmetry of the atmospheric model, we can use the relation $s = \sqrt{r^2 - b^2}$ to convert (6) to an integral in radius,

$$\Phi(b) = \frac{\pi}{f^2}\int_b^{r_{\max}} \mathrm{d}r \frac{2r}{\sqrt{r^2 - b^2}} n_e^2(r)K_{\mathrm{tel}}(t_e(r))\,, \tag{7}$$

where $r_{\max}$ is large enough that the X-ray flux from $r > r_{\max}$ is negligible, and b is the impact parameter of a particular line of sight with the Sun. Note that b is just measured distance on the film from the center of the image of the Sun, multiplied by 1 AU times the plate scale of the telescope. Modelling a plume as perpendicular to the Sun–Earth axis, with $r_{\mathrm{plume}} \ll r_\odot$ and $r_{\mathrm{plume}} \lesssim b$, the integral through the plume becomes trivial. We replace part of the atmospheric flux integral (7) with the X-ray flux emanating from the plume,

$$\Phi(b) = \frac{\pi}{2f^2}\left(\left(\frac{br_p}{r_\odot} n_{ep}^2(b)K_{\mathrm{tel}}(T_{ep}(b))\right) + \right.$$

$$\left. + \int_{\sqrt{b^2(1+(r_p^2/r_\odot^2))}}^{r_{\max}} \mathrm{d}r \frac{2r}{\sqrt{r^2 - b^2}} n_e^2(r)K_{\mathrm{tel}}(T_e(r))\right)\,, \tag{8}$$

where r_p is the radius of the plume at the limb of the Sun, and n_{ep} and T_{ep} are the electron density and temperature within the plume, respectively.

The observed plumes were modelled by numerically integrating the three equations of motion above and adjusting the initial conditions at the limb of the Sun, to fit the modelled X-ray flux to the observed image data by minimizing a normalized least-squares difference heuristic:

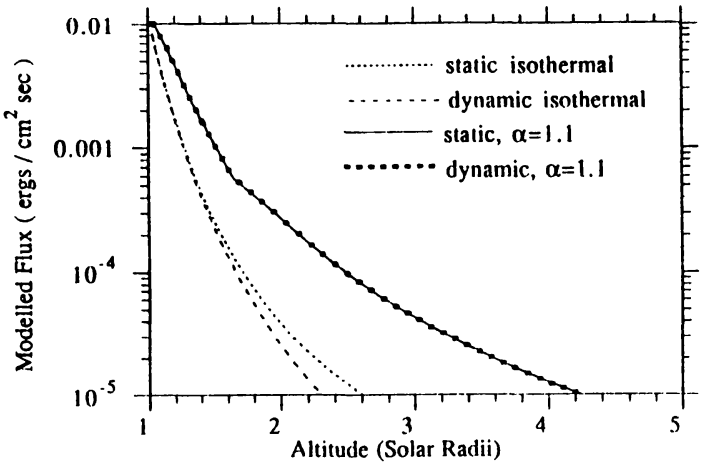

Fig. 7. Four model X-ray flux curves, as might be measured by our 173 Å Cassegrain telescope, observing a polar plume modelled four different ways. All four models have a base temperature of 2×10^6 K and a limb electron density of 1×10^9 cm^{-3}. Note that the predicted X-ray fluxes do not change significantly between the static and dynamic cases, below an altitude of 1.6 solar radii. Note also that, although the polytrope models have a shorter scale height than the isothermal, for this base temperature the telescope responds more strongly to the polytrope model. This is because the radial cooling of the polytrope plasma brings it within the telescope's response peak near 1×10^6 K.

$$H = \frac{1}{b_{\max}} \int_0^{b_{\max}} \frac{(\Phi_{\text{model}}(b) - \Phi_{\text{observed}}(b))^2}{(\Phi_{\text{observed}}(b))^2} \mathrm{d}b \,. \tag{9}$$

Both an isothermal ($\alpha = 1$ in Equation (5)) and a polytrope model with $\alpha = 1.1$ were used.

Velocity is determined in different ways for the isothermal and general polytropic case. In the isothermal case, Parker (1956) observed that, for any combination of initial density and temperature, there is exactly one solution to (2)–(5) that satisfies the necessary boundary condition of low velocity at the Sun and low pressure in the interstellar medium. However, in the case $\alpha > 1$, the single critical-velocity solution becomes a bounded set of velocities, all of which satisfy both the low- and high-altitude boundary conditions. Therefore, in the isothermal case, one can search for the single solution for which the acceleration is neither infinite nor zero at any finite radius; but in the case $\alpha = 1.1$, which most closely fits the observed coronal densities and temperature (Withbroe, Feldman, and Ahluwalia, 1991), the velocity is subject to the heuristic minimization process. Figure 7 shows the modelled fluxes from two typical coronal atmospheres, both with the same base temperature and density, but with differing velocity fields. From the fact that the two flux curves do not diverge significantly until an altitude of approximately 1.6 solar radii, we expect that our EYV flux data (which extend to approximately 1.5 solar radii) will not be particularly sensitive to velocity for this model.

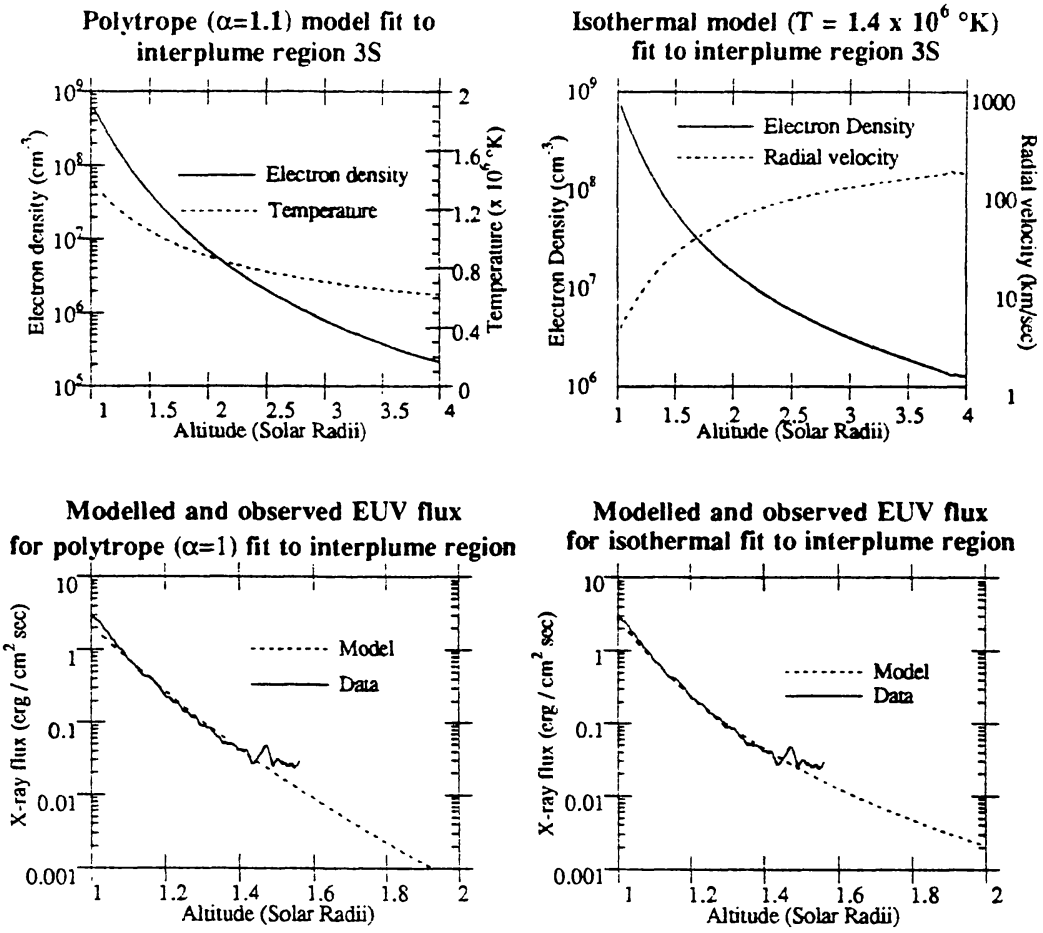

Fig. 8. Two models of the atmospheric background in Figure 3.

4. Results

The atmospheric part of the plume model should be constant across all of the observed plumes. Both an isothermal and a polytrope atmospheric background model were fitted to an inter-plume region, region 3 in Figure 3. The difference between an atmospheric and a plume model is that, for atmospheric X-ray/EUV emission, it is necessary to integrate the plasma's emissivity through successive layers of the coronal hole, as the line of sight passes by the Sun. Figure 8 shows the modelled parameters of this coronal hole for the two models, and compares the modelled and observed EUV fluxes. As expected, the polytrope fit was quite insensitive to velocity; thus, the isothermal model provides the only velocity information available. Figure 9 shows the variation of the least-squares fit with each parameter, for the polytrope model. Integrating the isothermal flow rate out to 1 AU yields a modelled solar wind velocity of 550 km s^{-1}.

Figure 10 shows two fits of our image data from a single plume, labelled region 1 in Figure 3. The atmospheric models shown in Figure 8 were used as background emission; the modelled EUV flux is the sum of the flux emitted by the plume

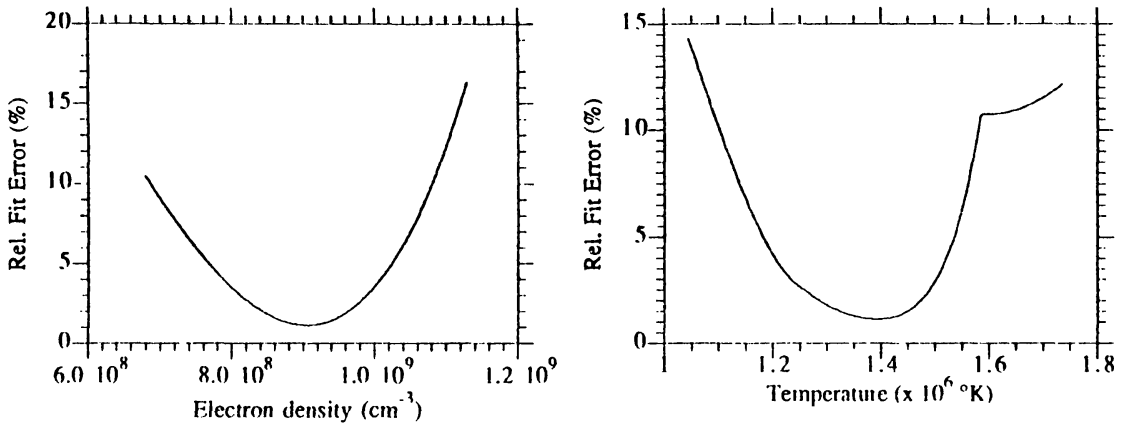

Fig. 9. Fit quality (H, defined in Equation (9)) vs parameter value, for the isothermal atmospheric fit in Figure 8. The electron density curve is for models with the best-fit temperature; the temperature curve is for models with the best-fit density.

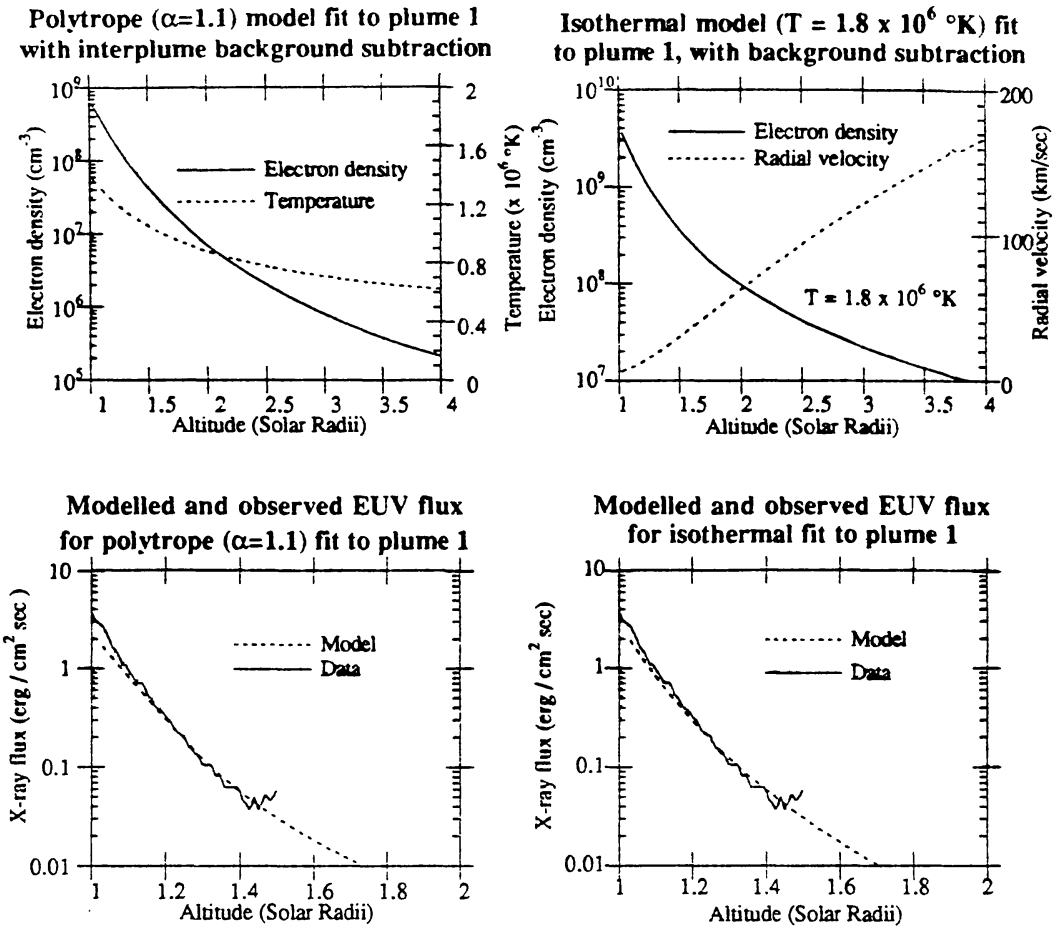

Fig. 10. Two models of a particular polar plume.

model, and that from the corresponding atmospheric background from Figure 8.

Integrating the isothermal plume model in Figure 10 yields a modelled wind velocity at 1 AU of 690 km s^{-1} at 1 AU, which is similar to that of observed

TABLE I
Fit parameters for the regions shown in Figure 3[a]

Plume No.	V_r at 1 AU (km s^{-1})	Temp. at limb ($\times 10^6$ K)	Density at limb ($\times 10^9$ cm^{-3})	Plume radius at limb (km)	Fit residual (%)
1	690	1.8	4.5	22 000	0.7
2	600	1.6	8.5	19 000	1.1
3 (atmos.)	550	1.4	0.91	n/a	1.2
4 (atmos.)	540	1.4	0.74	n/a	1.1
5	700	1.4	2.7	15 000	1.2

[a] Fit parameters for several plume and interplume regions near the south pole of the Sun, 23 October, 1987, using an isothermal Parker model as described in the text. Regions 3 and 7 are interplume atmospheric regions; regions 4, 5, and 6 are not shown because of their geometric ambiguity. The plume regions are background subtracted: region 3 was used as a background model for plumes 1 and 2, and region 7 was used as a background model for plume 8. Analysis of the variation of residuals with fit parameters suggests errorbars of 20% in temperature, 10% in density, and 20% in V_r at 1 AU.

high-speed wind streams. Figure 10(b) is a polytropic model with $\alpha = 1.1$. Again, velocity has been omitted from this graph, because the data cannot distinguish between different velocities at the observed altitudes. Because of the more rapid drop off of density with height, a higher base temperature is necessary than for the isothermal model. Table I shows the results of isothermal fits to several other plumes from this exposure.

5. Conclusions

We have demonstrated the power of X-ray/EUV multilayer telescopes as a quantitative plasma diagnostic in the solar corona, by fitting our observed data from 1987, with a simple model of polar plume expansion. Despite the lack of a direct quantitative measure of temperature or velocity in this data set, the high spatial resolution and low scattering of the multilayer telescope allows accurate modelling of scale height, and hence temperature and density, of the observed coronal plasma. Though the model we used is so simple as to prevent one from drawing conclusions about the origins of the solar wind, we note that extrapolating our observed coronal parameters to 1 AU yields numbers that are consistent with observed high-speed wind stream velocities.

With the higher resolution, higher contrast, better sensitivity, and direct temperature measurement capability of our later instrument, the Multi-Spectral Solar Telescope Array (MSSTA) telescope platform (Walker, Hooever, and Barbee, 1992b), it should be possible to constrain theories that explicitly model a heating and/or direct acceleration mechanism for polar plumes and other features of the corona, such as spicules, streamers, small loops, and bright points. By matching our image data with concurrent, ground-based visible-light coronagraph images,

such as those obtained by the National Center for Atmospheric Research at the High Altitude Observatory on Mauna Kea (Sime, 1988), we expect to accurately constrain more elaborate models of the corona – solar wind transition, not only for the polar coronal holes and plumes, but also for equatorial phenomena such as streamers, which are thought to be the source of the low-speed solar wind (Withbroe, Feldman, and Ahluwalia, 1991).

Acknowledgements

We wish to thank David Sime for his assistance in using the Eikonix microdensitometer at NCAR. We also wish to thank Richard Watts, Charles Tarrio, Mitchell Furst, and the rest of the SURF-II team for their assistance during our calibration measurements at NIST. This research is supported by NASA Grant NSG-5131 at Stanford and NASA/MSFC; Troy W. Barbee, Jr. was supported by DOE Contract W-7405-Eng-48.

References

Ahmad, I. A. and Webb, D. F.: 1978, *Solar Phys.* **58**, 323.
Ahmad, I. A. and Withbroe, G. L.: 1977, *Solar Phys.* **53**, 397.
Barbee, T. W., Jr.: 1985, in L. Chang and P. C. Gressin (eds.), *Synthetic Modulated Structures*, Academic Press, New York, p. 331.
Barbee, T. W., Jr.: 1989, *Proc. SPIE* **1159**, 638.
Bohlin, J. B., Sheeley, N. R., and Tousey, R.: 1978, *Space Res.* **15**, 651.
DeForest, C. E. *et al.*: 1990, *Opt. Eng.* **30**, 1126.
Doschek, G. A. and Cowan, R. D.: 1984, *Astrophys. J. Suppl.* **56**, 67.
Henke, B. L., Kwok, S. L., Vejio, J. Y., Yamada, H. T., and Young, G. C.: 1984, *J. Opt. Soc. Am.* **B1**, 818.
Hoover, R. B. *et al.*: 1988, *Kodak Tech Bits*, June 1988, p. 1.
Hoover, R. B. *et al.*: 1990a, *Proc. SPIE* **1343**, 175.
Hoover, R. B. *et al.*: 1990b, *Opt. Eng.* **29**, 1281.
Hoover, R. B. *et al.*: 1992, *Proc. SPIE* **1742**, 549.
Landini, M. and Monsignori Fossi, B. C.: 1990, *Astron. Astrophys. Suppl. Ser.* **82**, 229.
Lindblom, J. F. *et al.*: 1988, *Proc.SPIE* **982**, 316.
Malinovsky, M. and Héroux, L.: 1973, *Astrophys. J.* **181**, 1009.
Mewe, R., Gronenschild, E. H. B. M., and van den Oord, G. H. J.: 1985, *Astron. Astrophys. Suppl. Ser.* **62**, 197.
Parker, E. N.: 1956, *Astrophys J. Phys.* **128**, 664.
Parker, E. N.: 1963, *Interplanetary Dynamical Processes*, Interscience Publishers, New York.
Sime, D.: 1988, private communication.
Walker, A. B. C., Jr., Hoover, R. B., and Barbee, T. W., Jr.: 1992a, in J. Linsky (ed.), 'High Resolution Thermally Differentiated Images of the Chromosphere and Corona', *Advances in Stellar and Solar Coronal Physics*, Kluwer Academic Publishers, Dordrecht, Holland.
Walker, A. B. C., Jr., Hoover, R. B., and Barbee, T. W., Jr.: 1992b, *Proc. SPIE* **1742**, 500.
Walker, A. B. C., Jr., Barbee, T. W., Jr., Hoover, R. B., and Lindblow, J. F.: 1988a, *Science* **241**, 1781.
Walker, A. B. C., Jr., Lindblom, J. F., Hoover, R. B., and Barbee, T. W., Jr.: 1988b, *J. Physique Colloques C1* **49**, 175.
Walker, A. B. C., Jr. *et al.*: 1990, *Physica Scripta* **41**, 1053.

Withbroe, G. L.: 1986, in E. T. Hanssen, R. M. Wilson, and H. S. Hudson (eds.), *Solar Flares and Coronal Physics Using P/OF as a Research Tool*, NASA Conf. Publ. 2421, Greenbelt, MD, p. 221.

Withbroe, G. L., Feldman, W. C., and Ahluwalia, H. S.: 1991, in A. N. Cox, H. S. Livingston, and H. S. Matthews (eds.), *Solar Interior and Atmosphere*, University of Arizona Press, p. 1087.